Structure, Vol. 13, 637–648, April, 2005, ©2005 Elsevier Ltd All rights reserved. DOI 10.1016/j.str.2005.01.019

Crystal Structures of a Tetrahedral Open Pore Ferritin from the Hyperthermophilic Archaeon *Archaeoglobus fulgidus*

Eric Johnson,[1,*] Duilio Cascio,[2] Michael R. Sawaya,[2] Mari Gingery,[2] and Imke Schröder[1]

[1]Department of Microbiology, Immunology, and Molecular Genetics

[2]Department of Energy Laboratory of Structural Biology and Molecular Medicine

University of California, Los Angeles

Los Angeles, California 90095

Summary

Ferritins are known as important iron storage/detoxification proteins and are widely found in living organisms. This report details the 2.1 Å resolution native and 2.7 Å resolution iron bound structures of the ferritin from the hyperthermophilic Archaeon *Archaeoglobus fulgidus*, and represents the first structure of a ferritin from an archaeon, or a hyperthermophilic organism. The *A. fulgidus* ferritin (AfFtn) monomer has a high degree of structural similarity with archetypal ferritins from *E. coli* and humans, but the AfFtn quaternary structure is novel; 24 subunits assemble into a shell having tetrahedral (2-3) rather than the canonical octahedral (4-3-2) symmetry of archetypal ferritins. The difference in assembly opens four large (~45 Å) pores in the AfFtn shell. Two nonconservative amino acid substitutions may be critical for stabilizing the tetrahedral form.

Introduction

Iron is an essential element in the biological processes of virtually all organisms, and the capacity for iron to exist in multiple oxidation states makes it ideal as a biological cofactor. The only known organisms that have become iron independent are the Lactobacilli (Archibald, 1983), the lyme disease pathogen *Borrelia burgdorferi*, and the syphilis pathogen *Treponema pallidum* (Posey and Gherardini, 2000). Despite its usefulness, iron also presents serious problems for biological systems. Under aerobic conditions and at neutral pH, soluble ferrous iron (FeII) is spontaneously converted to the highly insoluble ferric (FeIII) form (10^{-18} M at pH 7), depleting iron from many biological environments. In addition, the interaction of oxygen and reduced oxygen species with iron can produce reactive oxygen species that are devastating to biological systems (Touati, 2000). Therefore, the need to store and tightly sequester iron in the cell became an important function for virtually all biological systems, and ferritins appear to be one of the evolutionary solutions to this problem.

Ferritin molecules are widely found in living systems, and the ferritin superfamily is comprised of a diverse group of proteins most commonly known to oxidize and store iron. The superfamily consists of three distinct subfamilies, which include the archetypal ferritins found in both Prokarya and Eukarya (Theil, 1987), the heme-containing bacterioferritins present only in bacteria (Carrondo, 2003), and the smaller Dps proteins only produced by Prokarya (Andrews et al., 2003). The role of iron storage has been firmly established and extensively studied in the archetypal ferritins from *E. coli* and higher Eukarya, including frogs, mice, and humans. In contrast, the physiological role of bacterioferritins remains less clear (Carrondo, 2003). Dps proteins were shown to bind DNA nonspecifically and are implicated in protecting DNA from oxidative damage in *E. coli* (Almiron et al., 1992). Other studies indicate that the *E. coli* Dps can store some iron (Zhao et al., 2002).

Crystal structures of ferritins from several aerobic bacteria and eukarya have been solved (Hempstead et al., 1997; Lawson et al., 1991; Stillman et al., 2001; Takagi et al., 1998). Only recently has the first structure of a bacterioferritin from an anaerobic organism, the bacterium *Desulfovibrio desulfuricans*, been solved (Macedo et al., 2003). Excluding the smaller Dps proteins that are comprised of 12 subunits, the quaternary architecture of all known ferritins is tetraeicosameric; 24 identical or similar polypeptides, each folded largely into a four helix bundle, are arranged with octahedral (4-3-2) symmetry forming a hollow protein shell with inner and outer diameters of approximately 80 Å and 120 Å, respectively. The inner central cavity can store up to 4500 FeIII atoms in the form of the crystalline mineral ferrihydrite (Theil, 1987). The archetypal ferritin sequesters this mineralized iron within a tightly closed protein shell which restricts the entry of reducing agents and controls the rate at which iron can be released from the molecule. The mechanism and route of iron release from ferritins remain uncertain although recent studies of eukaryotic ferritins have begun to shed light on these issues (Liu et al., 2003).

Archaeoglobus fulgidus is a strictly anaerobic, hyperthermophilic, sulfate-reducing, marine archaeon. The organism thrives in an extreme and dynamic environment located at the interface between superheated anaerobic vent fluids and frigid aerobic seawater. In contrast to most aqueous environments, vent fluids contain high concentrations (μM to mM) of free ferrous iron (Holden and Adams, 2003). However, transient exposure to oxygen or other iron reactive compounds such as H_2S present in the vent fluids could be lethal to the cell or lead to iron limitation.

In this work, we present the structure of the *A. fulgidus* ferritin (AfFtn) at 2.1 and 2.7 Å resolution for the native and iron bound proteins, respectively. Amino acid sequence comparison indicates that AfFtn is closely related to archetypal bacterial and eukaryotic ferritins. The X-ray crystallographic data presented here indicate that the metal ion binding mode, secondary and tertiary structure of AfFtn closely resemble those of bacterial and eukaryotic H-type ferritins. However, the tetrahedral quaternary structure of the *A. fulgidus* ferritin is unprecedented in its symmetry and in the presence of four large pores in the ferritin shell. The structures described here expand the current theories

*Correspondence: ericj@caltech.edu

Table 1. Data Collection and Refinement Statistics

	Se-Met			Iron
Derivative Dataset	Peak	Inflection	Remote	
Data collection				
Space group	$C222_1$			$C222_1$
Beamline/generator	ALS 8.2.2			Rigaku RU-200
Resolution (Å)	90.00–2.10	90.00–2.10	90.00–2.10	80.00–2.70
Wavelength (Å)	0.9797	0.9800	0.9720	1.5418
Total reflections	2,458,691	1,067,492	1,063,840	1,174,798
Unique reflections	175,814	174,236	174,631	86,172
Redundancy	14.0	6.1	6.1	13.6
Completeness (%)[a]	99.0 (100)	97.7 (99.6)	97.7 (99.5)	99.9 (100)
R_{merge} (%)[a,b]	7.7 (33.1)	6.9 (24.2)	6.7 (24.7)	9.7 (39.4)
I/σ (I)[a]	20.1 (5.7)	13.32 (5.2)	13.81 (4.6)	26.43 (6.7)
Refinement statistics				
Resolution (Å)		15–2.1		30–2.7
Number of atoms				
Protein		16,128		16,128
Metal		24 (Zn)		36 (Fe)
Water		871		531
R_{cryst} (%)[c]		17.8		17.7
R_{free} (%)[c]		21.8		21.7
Rms deviations				
Bonds (Å)		0.017		0.013
Angles (°)		1.57		1.46

[a] Numbers in parenthesis represent data in the highest resolution shell (2.10–2.18 Å for the Se-Met derivative, and 2.70-2.80 Å for the iron derivative).

[b] $R_{merge}(I) = \Sigma_{hkl}((\Sigma_i|I_{hkl,i} - [I_{hkl}]|)/\Sigma_i I_{hkl,i})$.

[c] $R_{cryst} = \Sigma_{hkl}|F_{obs}| - |F_{calc}/\Sigma_{hkl}|F_{obs}|$. R_{free} was computed identically, except that 5% of the reflections were omitted as a test set.

on iron entry and release from this family of protein multimers.

Results

Model Quality and Completeness

The 2.1 Å resolution native, and 2.7 Å resolution iron bound structures contain all but the first two N-terminal residues, and the last nine C-terminal residues due to local disorder in these regions. The electron density of both models was unbroken throughout except areas of low density in the D-E loops. In agreement with this, analysis of main chain B factors indicated the D-E loop region as an area with local mobility. Residue side chains with high solvent exposure exhibited relatively high temperature factors as would be expected. Ramachandran plots of the native and iron structures showed that 97.3%, and 96.1% of all residues were in the most favored regions, respectively, and that all residues adopted allowed rotamers. Crystallographic statistics are reported in Table 1.

The twelve subunits of the AfFtn asymmetric unit can be divided into two distinct conformational groups, distinguished by clear differences in D-E loop conformation (residues 146–150). These differences appear to be the result of different subunit packing interactions. Subunits A, D, E, G, I, and K belong to group 1, while subunits B, C, F, H, J, and L belong to group 2. Structural superpositioning of subunits using the program LSQMAN (Kleywegt, 1996) revealed an average root mean square deviation (rmsd) of 0.205 Å for 162 C^{α} in group1 versus group 2. Once these two groups were distinguished, noncrystallographic symmetry (NCS) restraints were applied to the two groups separately throughout the remainder of the model refinement process. Analogous conformational groupings have not been reported for other ferritin structures; instead, they are conformationally homogeneous.

Subunit Sequence and Structure Comparison

The amino acid sequence of the AfFtn shares 37% identity with *E. coli* ferritin A (EcFtnA) and 31% identity with human H ferritin (HuHf) (Figure 1). Hence, the fold of AfFtn is highly similar to the fold observed in these ferritins and is comprised of a canonical left-twisting four-helix bundle with a fifth short helix at the C terminus (Figure 2A). The remainder of the subunit is comprised of short loops connecting successive pairs of helices, with the exception of the B and C helices, which are connected by a long loop which spans the length of the molecule. As defined by hydrogen bonding (Kabsch and Sander, 1983), α helices A, B, C, D, and E are comprised of residues 6–35, 39–65, 85–113, 116–146, and 150–160, respectively (Figures 1 and 2A).

There are 25 residues that are strictly conserved within all three sequences (Figure 1), and these residues fall into three distinct groups. The first and largest group clusters in the hydrophilic core of the four-helix bundle. Five of the conserved residues in this central hydrophilic core (E19, E51, E52, H55, and E96) coordinate metal ligands in the AfFtn, EcFtnA, and HuHf structures, while AfFtn and EcFtnA share three additional residues (E128, E131, and E132) that provide metal coordination in this zone. Other strictly conserved residues in this region include Asn13 and 17, Gln15 and 128, and Tyr21, 26, and 125, which are likely important for establishing an appropriate environment for metal binding, ferroxidase activity, and transfer of

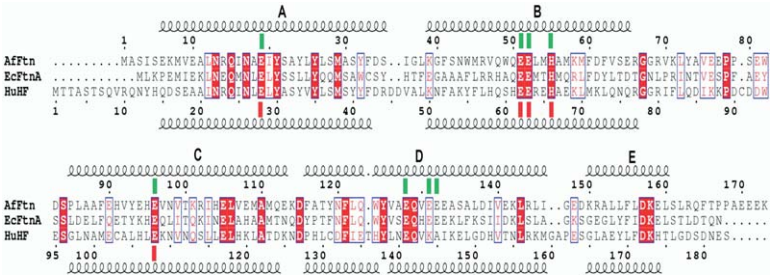

Figure 1. Structure-Based Sequence Alignment of the AfFtn, EcFtnA, and HuHf

Elements of secondary structure for the AfFtn and HuHf are shown above and below their respective sequences. White characters in a red background indicate strict conservation. Conservatively substituted residues are drawn in red and framed in blue while residues with poor conservation are drawn in black on a white background. Green rectangles above the AfFtn sequence indicate ferroxidase center residues in the AfFtn and EcFtnA. Red rectangles below the HuHF sequence indicate ferroxidase center residues for the human ferritin. Conservation scores were determined using the Blosum62 matrix. Alignments were made using CLUSTALX 1.81, and this figure was generated using ESPRIPT (Gouet et al., 2003)

iron ions into the protein's interior core. The strictly conserved tyrosine residues have been implicated in iron oxidation via an FeIII-tyrosinate complex or an intermediate tyrosine radical species in other ferritins (Pereira et al., 1997). The second group of conserved residues is located in the long BC loop. The amino acids in this group are involved in quaternary interactions at the 2-fold dimer interface, contributing to a network of amino acid side chains involved in hydrogen bonds, buried salt bridges, and hydrophobic interactions. The network of interactions seen in the AfFtn BC loop is similar to that observed in the HuHf structure, but bears even closer resemblance to the interactions which have been described in detail for the EcFtnA (Stillman et al., 2001). The low B factors for the residues in the AfFtn BC loop suggest a strong dimer interface. The third and final group of conserved residues appears to be important for defining boundaries of helical and loop regions. Notable are the conserved Gly67, and Ser84 residues that define the BC loop region. The conserved Gly147 also appears to define the end of the D helix in all three ferritins.

Structural superpositioning of ferritin monomers using the program LSQMAN revealed that AfFtn resembles EcFtnA more closely than HuHF. AfFtn subunit structures (NCS group 1) can be superimposed on EcFtnA and HuHf subunits with average rmsds of 0.849 and 1.09 Å for 158 C^{α} and 157 C^{α}, respectively (Figures 2B and 2C). Structural superpositioning of AfFtn subunits from NCS group 2 onto EcFtnA and HuHf subunits revealed average rmsds of 0.916 and 1.00 Å for 158 C^{α} and 155 C^{α}, respectively. The largest rmsds between both the prokaryotic subunits and the HuHf subunit lie in the D helix as well as in the AB and DE loops. As noted by Stillman et al. (2001), the D helix of HuHf contains a major bend caused by ϕ,ψ angle deviations in residues 124–125. The D helix in both prokaryotic ferritins contains a single deletion compared to the HuHf at position 124 and, therefore, has a more gradual turn.

When compared to HuHf, AfFtn has shorter loop regions in all of the loops except the long BC loop, which contains 19 residues in all three ferritins. Both prokaryotic ferritins have shorter loop regions in general, but the AfFtn loops are even more compact having one fewer residue in both the CD and DE loops than the EcFtnA. Compared to the HuHf, the AfFtn AB, CD, and DE loops are shortened by four, one, and two residues, respectively. The shorter loop regions seen in the AfFtn may be important for thermostablity (Vieille and Zeikus, 2001), while longer loops regions in eukaryotic ferritins like the HuHf may be required for the proposed pore gating mechanism at the 3-fold channels (Liu et al., 2003).

Subunit Packing and Quaternary Fold

Despite the high degree of similarity among the secondary and tertiary structures of AfFtn, EcFtnA, and HuHf, the quaternary structure of AfFtn differs strikingly from the other two. While in all previously known tetraeicosameric ferritin structures 24 subunits were ob-

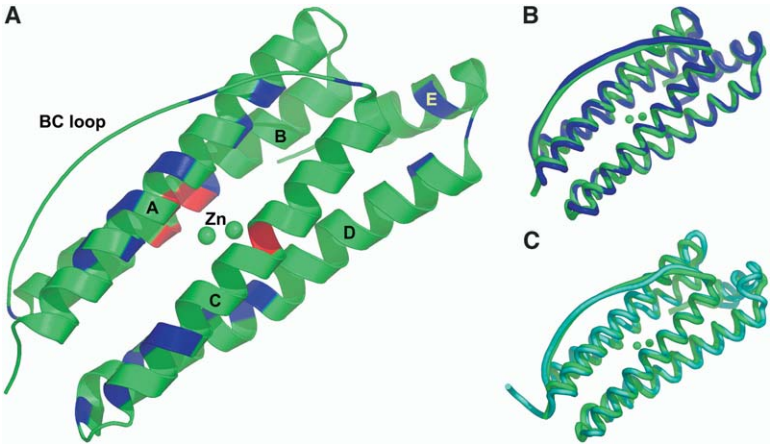

Figure 2. Subunit Structure of the AfFtn

(A) A cartoon ribbon representation of the AfFtn monomer (native structure) showing the location of the two bound Zn^{2+} ions. The model is colored green except for residues which are identical in the AfFtn, EcFtnA, and HuHf which are colored blue or red (red indicates conserved ferroxidase center residues).

(B) Tube-style cartoon representation of AfFtn structure (green) with EcFtnA (blue) structure superimposed (rmsd 0.849 Å, 158 C^{α}). The orientation of the AfFtn molecule is identical to that in (A).

(C) Structural superpositioning of AfFtn (green), and HuHf structures (rmsd 1.09 Å, 157 C^{α}). Images created using PYMOL.

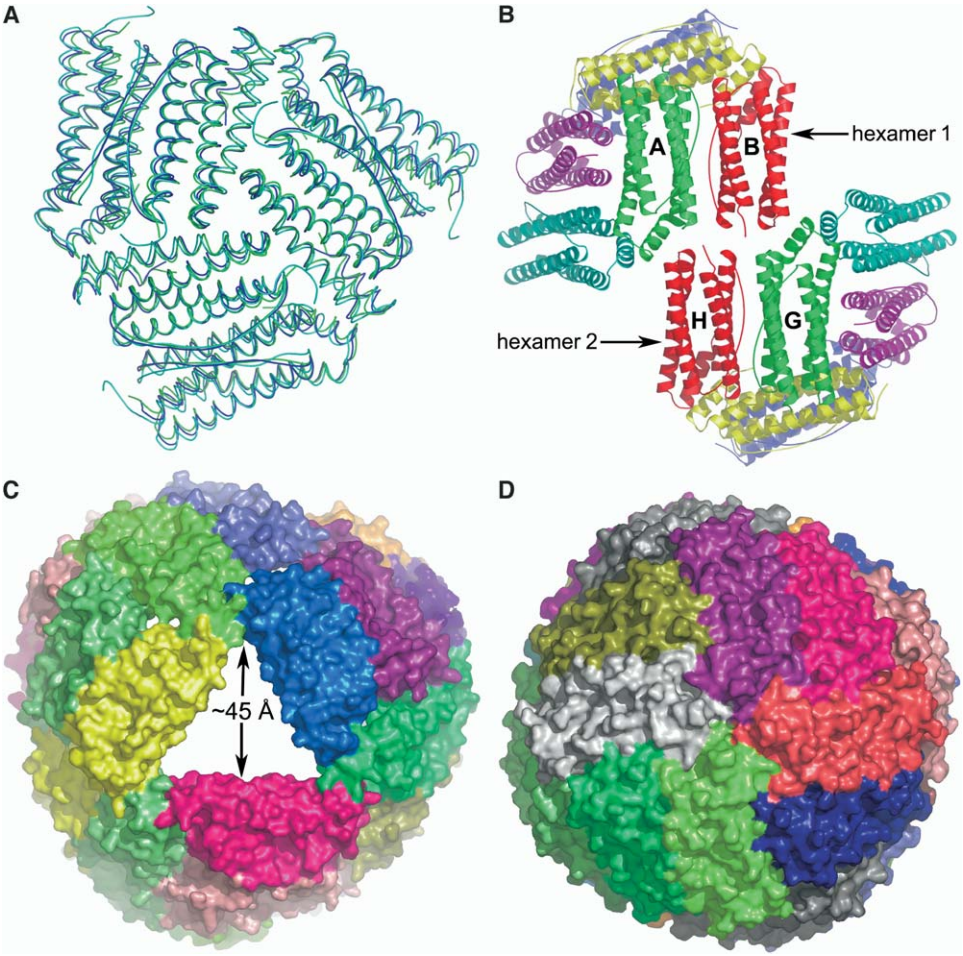

Figure 3. Quaternary Architecture of the AfFtn and Archetypal Ferritins

(A) Hexameric subassembly of the AfFtn (green tube-style cartoon ribbon) with hexameric assemblies from the EcFtnA (blue; PDB code, 1EUM), and HuHf (cyan; PDB code, 2FHA) superimposed. Superpositioning of structures using LSQMAN yields rms deviations from the AfFtn of 1.21 Å (860 Cα atoms), and 1.56 Å (893 Cα atoms) for the EcFtnA and HuHf, respectively.

(B) Cartoon ribbon model of the AfFtn asymmetric unit viewed down a noncrystallographic 2-fold symmetry axis showing the novel dodecamer interface. Symmetry related subunits in each hexamer are drawn in the same color for clarity.

(C) Surface representation of the novel tetraeicosameric assembly seen in the AfFtn. The molecule is viewed down one of four large pores at a 3-fold noncrystallographic symmetry axis.

(D) Surface representation of a closed archetypal tetraeicosameric ferritin shell (HuHf) viewed down a 4-fold molecular symmetry axis. Images created using PYMOL.

served to pack into tightly closed spherical shells with octahedral (4-3-2) symmetry (Figure 3D), the AfFtn assembles in a unique manner that results in a roughly spherical shell with tetrahedral (2-3) symmetry and containing four large pores. The large pores have an approximate 45 Å diameter resulting in roughly 2,500 $Å^2$ of pore area in the assembled tetraeicosamer (Figure 3C). Iron in form of Fe^{2+}, FeS_2, complexed iron, or substantially larger molecules, possibly carrying reducing equivalents, could potentially diffuse through these massive pores. The tetrahedral assembly also results in a less tightly packed shell having larger overall dimensions. A comparison of the internal cavity dimensions using the program VOIDOO (Kleywegt and Jones, 1994) indicates that the volume and average radius of the AfFtn internal cavity (324,900 $Å^3$, and 42.60 Å, respectively) are significantly larger than those of the EcFtnA (261,400 $Å^3$ and 39.56 Å) or HuHf (258,000 $Å^3$ and 39.53 Å).

The largest set of quaternary interactions shared in common between AfFtn and the archetypal ferritins corresponds to a hexameric assembly (Figure 3A), i.e., one-quarter of the tetraeicosameric shell. Structural superimposition of this AfFtn hexameric assembly with that of EcFtnA, or HuHf using LSQMAN yields relatively small rmsds of 1.21 Å (860 C^α atoms) and 1.56 Å (893 C^α atoms), respectively (Figure 3A). Thus, the small 3-fold symmetric channel formed at the center of each hexamer is conserved among all three ferritins (Figure 3A). There are two copies of this hexamer in the AfFtn asymmetric unit (Figure 3B). Hexamer 1 is comprised of subunits ABCDE&F, with hexamer 2 consisting of subunits GHIJK&L.

The principal architectural difference between the

Table 2. Hydrogen Bonds at the Hexamer 1–Hexamer 2 Interface

Hexamer 1 Atom	Solvent Atom	Hexamer 2 Atom	Distance (Å)	Distance (Å)
LysA150NZ	None	MetH111O	2.83	
Arg F151NE	WAT 440	Tyr H 119OH	3.01[a]	2.83[b]
ArgA151NH2	WAT 856	GlnH123OE1	2.64[a]	2.97[b]
AspA157OD2, LeuA154O	WAT807, WAT807	AsnH151ND2	2.53[a] 3.17[a]	310[b]
IleA36O	WAT 705	LysH114O	2.64[a]	2.78[b]

Hydrogen bonds are listed for only one of the two symmetry related pairs at the hexamer1–hexamer 2 interface.
[a] Hexamer 1 atom to solvent atom distance.
[b] Hexamer 2 atom to solvent atom distance.

tetrahedral and octahedral symmetries can be described almost entirely by differences in how the hexameric assemblies are joined to form the tetraeicosamer. In HuHf and EcFtnA, the hexamers are joined by 4-fold symmetry elements. In AfFtn, the hexamers are joined by 2-fold symmetry. Specific amino acid residues at the hexamer–hexamer assembly appear to govern whether 4-fold or 2-fold symmetry will form. In AfFtn, the interface between hexamer 1 and hexamer 2 involves contacts between subunits A and B in hexamer 1 with subunits G and H in hexamer 2 (Figure 3B). The side chain amine of LysA150 (hexamer 1) forms a hydrogen bond with the backbone O at MetH111 in hexamer 2. Identical hexamer 1–hexamer 2 contacts are formed between symmetry-related LysB150 NZ and MetG111 O. In the assembled tetraeicosamer, a total of 12 such interactions exist. Additional solvent mediated hydrogen bonds that appear to stabilize the tetrahedral assembly exist at the hexamer interface (Table 2). Finally, nonpolar residues LeuA38, LeuA153, and LeuA154 (hexamer1) form a hydrophobic pocket that surrounds the PheH116 and MetH111 side chains of hexamer 2. The presence of hydrophobic contacts at the hexamer–hexamer interface is consistent with observations that proteins from hyperthermophilic organisms tend to be stabilized by hydrophobic interactions (Vieille and Zeikus, 2001). Furthermore, gel filtration experiments at varying NaCl concentrations indicate that hydrophobic interactions are important for stabilization of the AfFtn tetraeicosamer. For example, at NaCl concentrations of 150 mM or above the apo-AfFtn elutes as a tetraeicosamer. At low ionic strengths (NaCl concentrations of 20 mM or less) the apo-AfFtn exists largely as a dimeric species. Holo-AfFtn elutes as a tetraeicosamer even at low ionic strength suggesting that the tetraeicosamer is also stabilized by the iron core (Table 3; and see the Supplemental Data available with this article online).

Table 3. Molecular Weight of the AfFtn in Solutions of Various Ionic Strengths

	Percent of Protein Observed at Given Molecular Weight	
[NaCl] (mM)	45 kDa	490 kDa
20	95	5
150	5	95
300	5	95
600	0	100
20 (mineralized)[a]	0	100

[a] AfFtn mineralized with 500 Fe/tetraeicosamer (see Experimental Procedures for details).

There are also differences in orientation of the E helix in both prokaryotic ferritins when compared to the HuHf. In the EcFtnA tetraeicosamer the N-terminal ends of the E helices are located close together near the outer surface of the molecule but the C termini of the E helices point away from the symmetry axis creating a channel which widens toward the inside of the molecule (Stillman et al., 2001). In contrast, the E helices of HuHF and other animal ferritins lie roughly parallel with the tetraeicosameric 4-fold axis (Ha et al., 1999; Hempstead et al., 1997). The AfFtn E helix adopts an orientation nearly identical to that of the EcFtnA but is positioned slightly further toward the 3-fold symmetry axis in the AfFtn tetraeicosamer.

The unusual tetrahedral quaternary structure of the AfFtn gives rise to the question of whether this packing could be stabilized as result of crystal contacts and, therefore, be an artifact of crystallization, primarily involving the hexamer–hexamer interface. In addition to the size exclusion chromatography discussed above, electron microscopy was used with the aim of determining whether preformed tetraeicosamers were present in solutions containing purified mineralized AfFtn (Figure 4). The AfFtn clearly appears as assembled tetraeicosamers, which argues strongly against the possibility of aberrant tetraeicosamer formation in crystals due to crystal lattice constraints. Furthermore, the images suggest that AfFtn tetraeicosamers are catalytically active and can form a mineral iron core as molecules with and without dark cores can be seen and correspond to holo- or apo-ferritin molecules, respectively (Figure 4A and inset). In a positive control, both apo- and holo-ferritin forms of the horse spleen ferritin appear as fully assembled tetraeicosamers (Figure 4B and inset).

Ferroxidase Center

Zinc

Two metal ions (Zn1 and Zn2) have been modeled in the ferroxidase center of the native crystal structure (Figures 5A and 5C). Several lines of evidence suggest that the metal ions at this location are most likely Zn. AfFtn produced in and purified from *E. coli* was virtually devoid of iron. Determination of the iron content in purified AfFtn indicated 0.5 mol of iron per mol of tetraeicosamer. In addition, anomalous difference Fourier analysis of data from native protein crystals collected at the copper Kα wavelength (1.5418 Å) showed no peaks at the ferroxidase center. The lack of anomalous signal at this wavelength excludes Mn, Fe, and Co as candidates for these ions (data not shown). A second phased

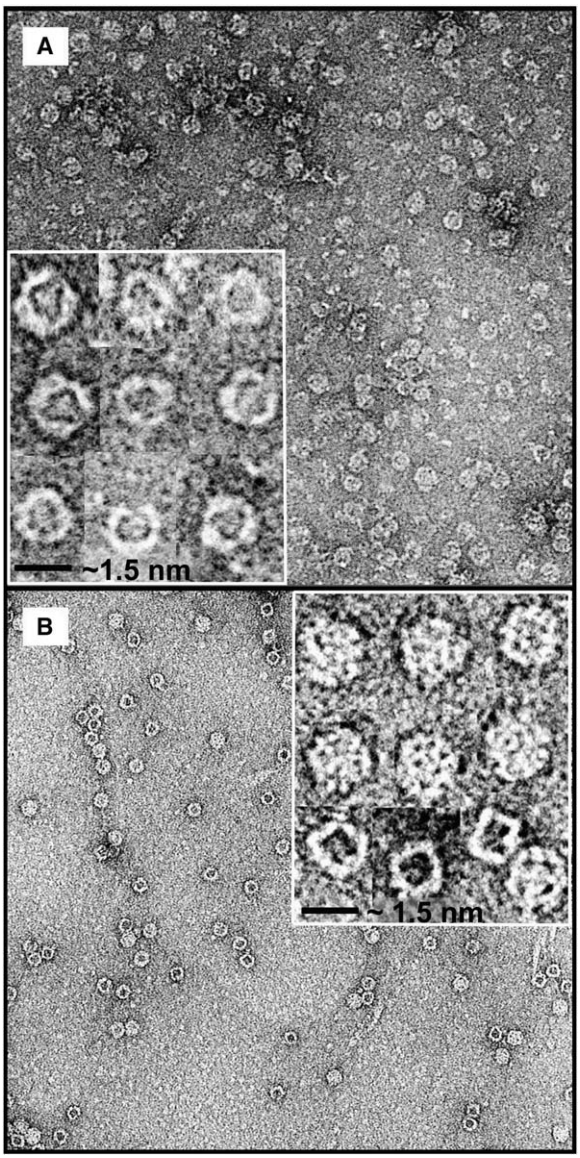

Figure 4. Electron Micrographs of Mineralized Samples of the AfFtn, and an Archetypal Eukaryotic Ferritin (Horse Spleen)

(A) Micrograph of mineralized AfFtn reveals that fully assembled tetraeicosamers of apo- and holo-ferritin exist in solution. Examination of a selected collection of holo-ferritin molecules (dark centers) in greater detail illustrates the presence of iron within the core (inset, Figure 6A).

(B) A solution of mineralized horse spleen ferritin also contains fully assembled tetraeicosamers which exist in both the apo- and holo-ferritin forms. Inset shows a selected collection of both forms of the horse spleen ferritin.

anomalous difference Fourier analysis of data from native protein crystals collected at 0.972 Å (Table 1) showed peaks (> 3 sigma) at the ferroxidase center. These anomalous peaks are consistent with the presence of a transition metal such as Zn, Cu, or Ni. However, they exclude Mg, which is present in the crystallization buffer. The presence of Zn at these sites is also consistent with Zn binding sites identified in EcFtnA (Stillman et al., 2001). In AfFtn, Zn1 is coordinated by three protein ligands (Glu19 OE1, His55 ND1, Glu52 OE1), a Zn1-Zn2 bridging ligand, and two water ligands (W729, and W356). Zn2 has four ligands contributed by the protein side chain atoms Glu52 OE2, Glu96 OE1 and OE2, and Glu132 OE1, the Zn1-Zn2 bridge and the solvent ligand W356. The average Zn1-Zn2 distance of 2.85 Å is significantly shorter than the Zn1-Zn2 distance of 3.43 Å observed in the EcFtnA zinc derivative, suggesting that the zinc ions may occupy either site alternatively, but not simultaneously. During the course of refinement occupancies of 0.4 and 0.3 were assigned to Zn1 and Zn2, respectively. Taking the water ligands into account, both the Zn^{2+} ions are six coordinate or have an approximate octahedral coordination.

Iron

Examination of the electron density observed after addition of ferrous sulfate to the native crystals under aerobic conditions revealed several changes in the iron derivative when compared to the native structure. Most striking were the presence of three large (>7 sigma) peaks of electron density located at the ferroxidase center of each subunit. These peaks were seen in the anomalous difference Fourier maps (Figure 5D) and allow for an unambiguous assignment of iron ions at these positions. Two of the peaks largely coincided with the Zn1 and Zn2 positions within the hydrophilic interior of the four-helix bundle and have been assigned to Fe^{3+} ions labeled Fe1 and Fe2, respectively. A third peak, assigned to Fe3, is located an average of 5.96 Å from Fe2 near the interior surface of the protein shell.

Protein ligands coordinating the Fe1-Fe2 pair are equivalent to those coordinating the Zn1-Zn2 pair in the native structure with only minor side chain movements occurring upon iron binding (Figures 5C and 5D). Fe3 is coordinated by Glu51 OE2, Glu128 OE2, Glu131 OE1, and Glu132 OE2. Binding of this third iron atom requires substantial rotation of the Glu51 and Glu131 side chains. Prior to iron binding, the Glu51 and Glu131 side chains are oriented pointing inwards toward the ferritin core. Rotation about the chi1, chi2, and chi3 dihedrals results in reorientation of these side chains inward toward the third metal site and toward the interior of the four-helix bundle, movements that suggest a gating mechanism for transfer of iron out of the ferroxidase center and into the interior core. Similar rearrangements of the Glu51 and Glu131 side chains have been observed between the EcFtnA iron and zinc derivatives (Stillman et al., 2001). The authors suggested that His48, which adopts a different conformation in the native versus metal bound structures, may be important for the required stereochemical alignment of Glu128 for metal binding and/or ion gating into or out of the metal binding sites. While His48 is conserved in other bacterial nonheme ferritins, AfFtn and HuHf contain Gln at this position, indicating that iron binding and or gating is not strictly dependent on a histidine side chain at this position.

Due to the lower resolution data for the iron derivative, solvent molecules were not clearly defined and were therefore not modeled into the metal coordination sphere. In fact, the electron density surrounding the iron ions likely has contributions from solvent molecules or the expected bridging peroxo and or oxo inter-

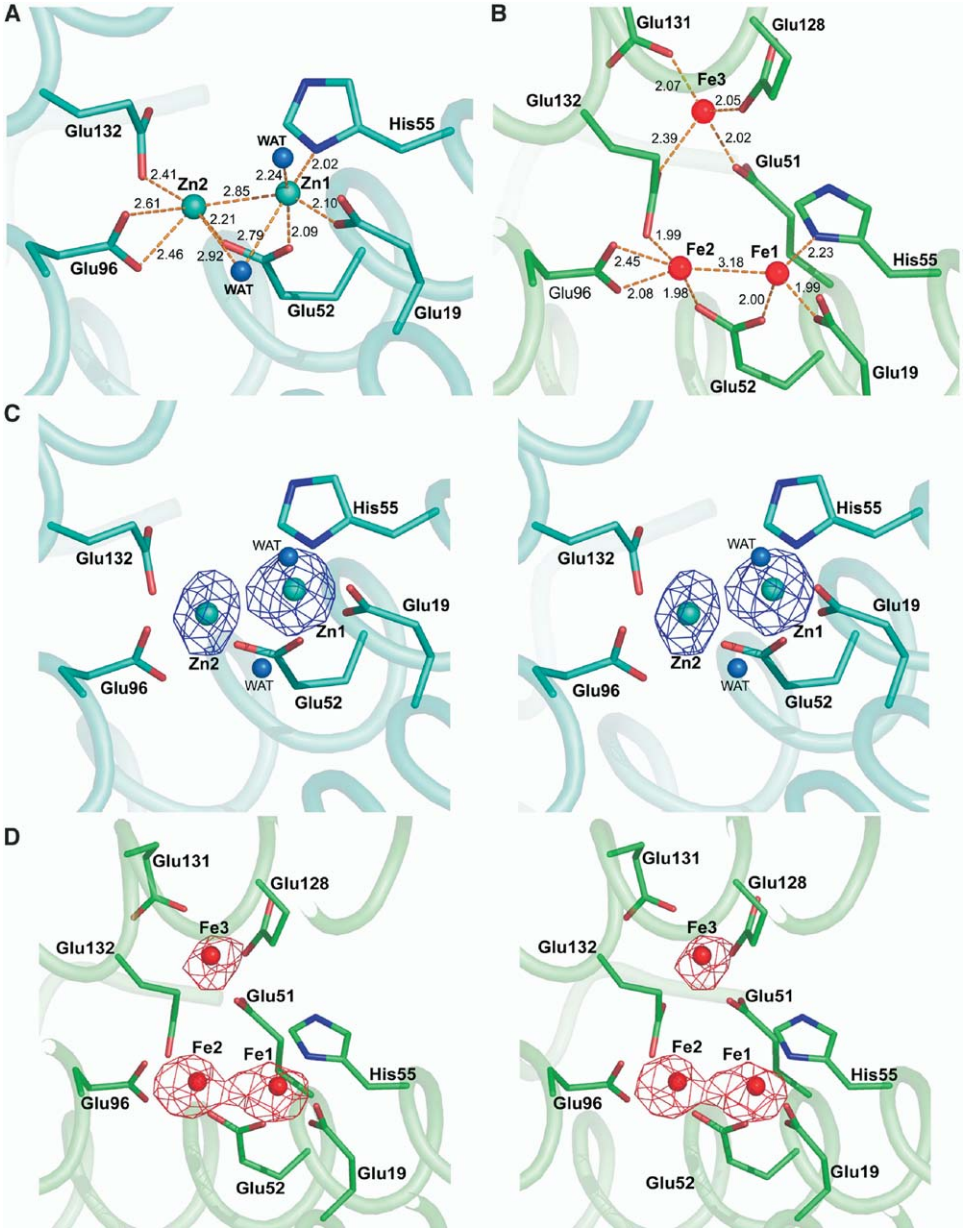

Figure 5. The AfFtn Ferroxidase Center

Bond lengths (Å) are averaged from the 12 crystallographically independent subunits in the asymmetric unit.

(A) Schematic representation of the Zn^{2+} bound structure depicted in CPK color. Carbon atoms are shown in cyan, nitrogen atoms in blue, and oxygen atoms in red. Zn^{2+} ions and solvent molecules are shown as cyan and blue spheres, respectively. Dashed lines illustrate the approximate octahedral coordination of the metal atoms.

(B) Schematic of the Fe^{3+} bound structure. Coloring scheme is identical to (A), except carbon atoms are drawn in green and Fe^{3+} ions are shown as red spheres.

(C) Stereo view of the Zn^{2+} bound structure ferroxidase center. $F_o - F_c$ difference electron density contoured at 5 sigma (cyan mesh) is shown for the Zn1 and Zn2 sites.

(D) Stereo view of the Fe^{3+} bound ferroxidase center. Anomalous difference Fourier electron density (red mesh) contoured at 6.5 sigma allows for an unambiguous identification of iron ions at these positions.

mediate ligands seen in other high-resolution ferritin structures, and this ambiguity is reflected in the relatively high average temperature factors of 43.40, 46.01, and 49.43 $Å^2$ for the Fe1, Fe2, and Fe3 sites, respectively. Considering the lower resolution data, it is difficult to assign complete coordination to the iron atoms.

At the limit of the 2.7 Å resolution data, the binding mode of the AfFtn appears nearly identical to that seen in the EcFtnA structure, and, therefore, metal coordination is also likely to be similar in the two proteins. The average Fe1-Fe2 distance of 3.18 Å seen in the AfFtn structure compares closely with the distance of 3.24 Å

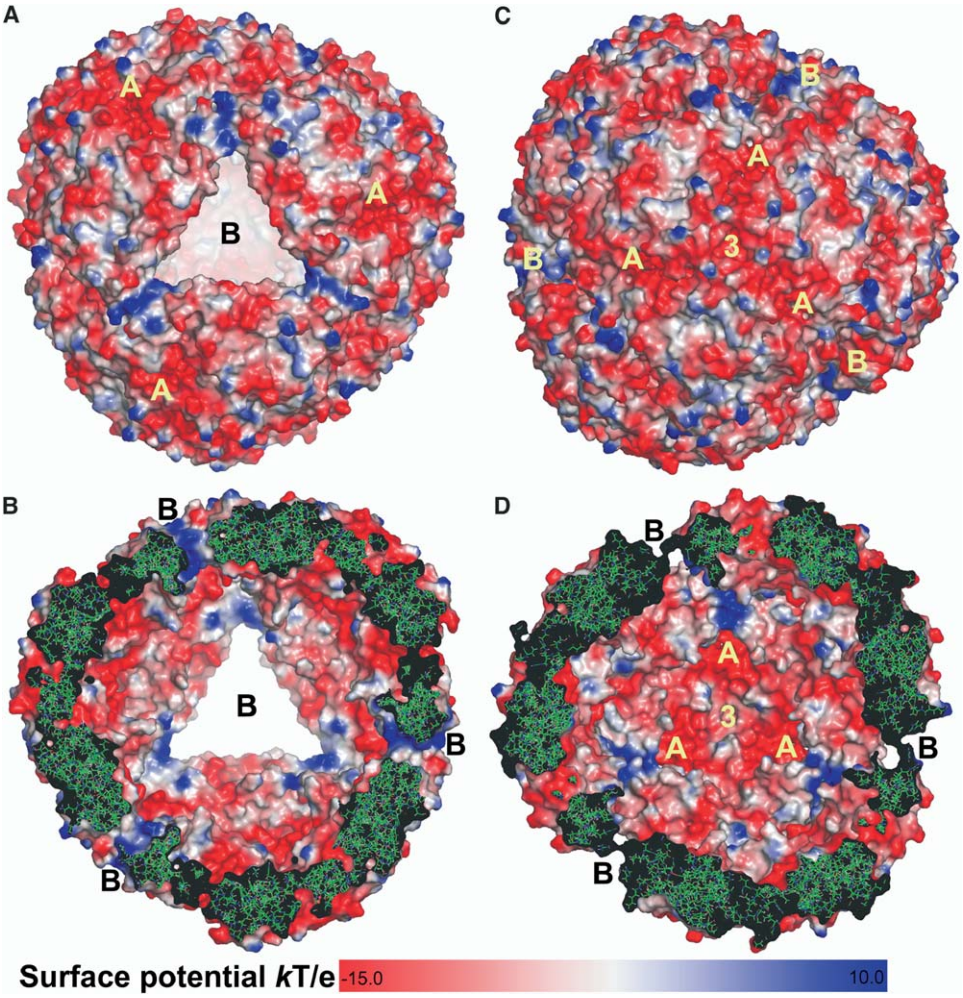

Figure 6. Electrostatic Potentials on the Surfaces of the AfFtn

(A) External surface view down one of the four large pores.

(B) Internal surface view facing up the large pore.

(C) External view down a noncrystallographic 3-fold symmetry axis.

(D) Internal view up a 3-fold noncrystallographic axis. "A" indicates the minor channel, "B" the large pore, and "3" represents a 3-fold noncrystallographic axis. Protein below the molecular surface is depicted as green sticks. Molecular surfaces were calculated using PYMOL using a probe radius of 1.4 Å. Electrostatic potentials were calculated using UHBD (Davis et al., 1991). Calculations were based on protein and solvent dielectric constants of 4 and 80, respectively, an ionic strength of 0.13 M, and a temperature of 298 K.

seen in the EcFtnA iron derivative. The similarity of the average Fe2-Fe3 distances of 5.96 Å and 5.79 Å for the AfFtn and EcFtnA iron derivatives, respectively, also illustrates the similarity of the iron binding mode in these two ferritins.

Surface Electrostatic Potentials

Examination of the internal and external surfaces of the AfFtn tetraeicosamer reveals a prevalence of residues that carry a negative charge, and this has also been described for other ferritins (Carrondo, 2003; Macedo et al., 2003; Theil, 2001). Calculation of the electrostatic potentials on these surfaces emphasizes potential routes for movement of ions or larger molecules through the AfFtn shell.

Each of the AfFtn's four large pores provides an approximate 600 $Å^2$ area through which ions or much larger molecules could pass, and represents a novel route to or from the ferritin interior. The entrance to the four large, triangular-shaped pores (designated B in Figure 6) is accentuated by clusters of positive surface potential located at the triangle apices (Figures 6A and 6B). This positive electrostatic potential extends from the exterior surface, through the pore opening, and onto the interior surface of the AfFtn shell. This arrangement of electrostatic potential appears well suited for promoting interaction with negatively charged species, and results from the Lys150, and Arg151 residues unique to AfFtn, which are localized to the B pore apices by convergence of E helices from two distinct subunits.

Despite the presence of the four large pores in the AfFtn tetraeicosamer, a second potential route for entry of ions into the ferritin core exists at negatively charged

channels (designated A in Figure 6). These channels are located between the 3-fold noncrystallographic symmetry axis and the large "B" pores and are distinct from the 3-fold channels. The "A" channels extend to the interior of the protein shell and are sufficiently large to allow the passage of iron ions. Analogous channels have been reported in studies of prokaryotic ferritins, including EcFtnA, where they have been suggested as a route for specifically funneling positively charged iron ions to the internal mineralization site after ferroxidase center mediated nucleation of the ferrihydrite mineral has occurred (Macedo et al., 2003). In contrast to the AfFtn and bacterial ferritins, these "A" channels have not been observed in eukaryotic ferritins. In HuHf, for example, iron is thought to enter through channels at the 3-fold axis which are characterized by a negatively charged outer surface that is surrounded by clusters of positively charged potential (Chasteen and Harrison, 1999).

Discussion

The quaternary structure of the AfFtn reported here reveals a novel tetrahedral symmetry and the formation of four large open pores in the protein shell. The unique architecture appears to represent a biologically relevant form of the assembly rather than being an artifact of heterologous expression, heat purification, selenomethionine substitution, or crystallization. Functional and structural studies of mesophilic bacterial and eukaryotic ferritins routinely use heterologously expressed and heat purified proteins (Ha et al., 1999; Hudson et al., 1993; Santambrogio et al., 2000). AfFtn prepared in this manner appears to be folded properly as the AfFtn fold is very similar to both EcFtnA and HuHf. Furthermore, electron micrographs reveal that AfFtn can assemble into tetraeicosameric shells that are capable of oxidizing ferrous iron and producing iron cores. The substitution of selenomethionine for methionine evidently plays no role in producing the tetrahedral symmetry as the native protein also crystallizes with the same tetrahedral symmetry (data not shown). Gel filtration and electron microscopy analysis (Figure 4; Table 3) suggest that the AfFtn tetraeicosamer is assembled under the high ionic strength conditions used for crystallization. However, considering the observation of an equilibrium between dimeric and tetraeicosameric species in gel filtration experiments, it is plausible that an equilibrium exists between the open pore tetrahedral shell, and a hypothetical closed octahedral shell resembling that of archetypal ferritins like EcFtnA, and HuHf. Structural interconversion could occur either through dissociation into a dimer or through reorientation of hexamers within the shell. Since *A. fulgidus* thrives at a salt concentration of about 0.5–0.6 M and accumulates osmotically active compounds to match the external ionic strength (Martins et al., 1997), an equilibrium between open and closed AfFtn tetraeicosamers seems less likely to occur in vivo. Further studies are needed to determine if such an equilibrium occurs, and if it is biologically relevant.

Amino acid substitutions in helix E of AfFtn compared to EcFtnA and HuHf might explain why AfFtn adopts a tetrahedral architecture while the other ferritins are octahedral. Helix E resides at the interface of the 4-fold symmetry axes of EcFtnA and HuHf, and it is precisely this interface that is broken to form the tetrahedral symmetry of the AfFtn tetraeicosamer. Structural superpositioning of the AfFtn monomer on the EcFtnA octahedral complex (using LSQMAN) reveals that Arg151 would sterically hinder AfFtn monomers from associating with a 4-fold symmetry analogous to human and *E. coli* ferritins. In the octahedral EcFtnA and HuHf complexes, the structural equivalents of Arg151 are a glutamate and leucine residue, respectively. In the octahedral complexes, the nonpolar residues of neighboring subunits pack together with 4-fold symmetry, but the extended length and positive charge of an arginine at this position would likely inhibit association of subunits through 4-fold symmetry.

The Lys150 position corresponds to the first residue of the E helix and replaces a glycine residue in both the EcFtnA and HuHf. The Lys150 side chain participates in hydrogen bonds which stabilize the AfFtn's tetrahedral assembly (results and Table 2). Therefore, Lys150 and Arg151 seem critical as they contribute to the stabilization of the tetrahedral assembly, and to the destabilization of the octahedral form, respectively. Furthermore, both Lys150 and Arg151 may have some functional significance as they establish the cluster of positive electrostatic surface potential observed at the B pore apices. Replacement of these residues using site directed mutagenesis is currently underway.

As a deep sea hydrothermal vent organism, *A. fulgidus* inhabits a turbulent environment with a steep temperature gradient. Various nutrient, metal ion, and gas gradients exist that are affected by the thermal vent dynamics and the biological activity of the microbial vent community. In this rapidly changing environment, organisms such as *A. fulgidus* transiently encounter soluble Fe^{2+}, H_2S, and oxygen. To avoid production of reactive oxygen species via the Fenton reaction and/or to avoid spontaneous formation of ferric oxide or ferric sulfide precipitates within the cell, *A. fulgidus* would require a mechanism to rapidly sequester iron. Currently, we can only speculate that the open pore AfFtn represents a mechanistically simple ferritin that evolved as an adaptation to the dynamic hyperthermophilic niche in which *A. fulgidus* thrives. The large B pores may simply provide a static, ungated route for the entry/release of iron ions, iron sulfides, or molecules carrying reducing equivalents. Therefore the AfFtn's open pore structure appears to provide the organism with a relatively simple structural solution to the problems of iron storage and toxicity which are unique to its environment. However, the precise nature of the physiological iron species, reducing molecules, and the physiological oxidant for the ferroxidase reaction of *A. fulgidus* remain to be established.

Experimental Procedures

DNA Cloning, Protein Preparation, and Crystallization

The 522 base pair (bp) *A. fulgidus* ferritin gene (AF 0834) was PCR cloned from genomic DNA template using pfu DNA polymerase, gene-specific primers, including NdeI and EcoRI restriction sites and inserted into the pET11a expression vector (Novagene). Native

and selenomethionine-labeled protein was produced in *E. coli* strain BL21 (λDE3) codon plus (RIL). Selenomethionine-labeled protein was produced using the method of metabolic inhibition (Doublie, 1997). Heat treatment of lysed cells (85°C, 10 min) was followed by centrifugation to remove insoluble material and liquid chromatography using a 24 ml phenyl sepharose column (Pharmacia) which yielded full-length, wild-type AfFtn. The iron content of the purified recombinant protein was determined as the 2-2′ bipyridyl complex at 520 nm (Bothwell and Mallett, 1955). Initial crystals were identified after about 1 week (Crystal Screen 1; Hampton Research) using the hanging drop vapor diffusion method. Optimization of crystallization was then performed using microbatch (Chayen et al., 1990) and modified microbatch (D'Arcy et al., 1996) under paraffin oil (Fisher Scientific), or a 1:1 ratio of paraffin oil and silicon oil (Dow Corning), respectively, in 72-well microbatch plates (Hampton Research). The optimized crystallization drops consisted of 27.4% PEG 400, 0.15 M $MgCl_2$, 0.1 M HEPES (pH 7.5), and a final protein concentration of 13.1 mg/ml. Orthorhombic crystals of AfFtn (space group $C222_1$; a = 183.437 Å, b = 187.831 Å, c = 178.089 Å; V_M = 3.40 Å^3/Da for 12 monomers per asymmetric unit) of approximately 0.5 × 0.5 × 0.3 mm appeared within 4 to 7 days at 25°C, and diffraction data extended to ~2.8 Å. To improve X-ray diffraction resolution, crystallization drops were covered in 100% silicon oil to allow for rapid passage of water vapor, and dehydrated for 5 days (Esnouf et al., 1998; Schick and Jurnak, 1994). The structure reported here was solved by multi-wavelength anomalous diffraction (MAD) phasing of the selenomethionine derivative. The iron derivative was produced by direct addition of small $FeSO_4$ crystals into crystallization drops prepared identically to that of the selenomethionine derivative. Crystals acquired a reddish tinge upon soaking. Crystals in these drops were allowed to soak for 30 min before harvest and immediate freezing in a nitrogen stream. Dehydration of crystals soaked in $FeSO_4$ was not performed resulting in slightly larger unit cell dimensions for these crystals (a = 184.504 Å, b = 190.245 Å, c = 179.408 Å).

Data Collection, Phasing, and Refinement

Synchrotron data of the selenomethionine derivative were collected at 105 K on the Lawrence Berkeley National Laboratory—Advanced Light Source, beamline 8.2.2. Data for the iron bound structure were collected at 105K on a Raxis IV area detector using a Rigaku RU-200 generator at the UCLA-DOE Institute for Genomics and Proteomics X-Ray Crystallography Core Facility. Data were processed with DENZO/SCALEPACK (Otwinowski and Minor, 1997), and MAD phasing proceeded by the standard methods of heavy atom location (SHELXD [Schneider and Sheldrick, 2002]), maximum likelihood phase refinement (MLPHARE [CCP4, 1994]), and density modification (DM [Cowtan and Main, 1998]). Fifty of the 108 possible Se sites in the asymmetric unit were located using the anomalous differences collected at the peak wavelength of 0.9797 Å (Table 1). Phases calculated to 2.10 Å resolution yielded high-quality maps, which permitted manual fitting of a model of a single subunit constructed using the web based 3D-PSSM protein fold recognition server (Kelley et al., 1999) based on the AfFtn amino acid sequence, and the protein structure having the highest sequence identity (*Campylobacter jejuni* metal binding protein; PDB code, 1KRQ). Initial fitting of the remaining 11 subunits was performed using a combination of manual and automated rigid body refinement methods.

Model building and refinement were done using O (Jones et al., 1991) and REFMAC5 (Murshudov et al., 1999), respectively. Location of solvent atom positions was performed using the ARP option in REFMAC5 (Perrakis et al., 1999). Superpositioning of individual monomers led us to conclude that the twelve molecules in the asymmetric unit fell into two conformationally distinct groups. Therefore, in subsequent stages of refinement, separate noncrystallographic symmetry restraints combined with TLS (Winn et al., 2001) refinement parameters were used for these two groups. Refinement rounds ended with inspection of the model and σA-weighted $2F_o - F_c$ and $F_o - F_c$ maps. The final native model consists of an AfFtn dodecamer (12 protein chains, labeled A–L), 871 solvent atoms (HOH), and 24 zinc atoms (ZN). The refined native structure (excluding solvent and metal atoms) was then used as a starting model for refinement of the iron bound structure. The final iron bound model contains 36 iron atoms (FE) and 531 solvent atoms (HOH). The occupancies of the Zn atoms were adjusted until the isotropic B factors would match more closely the average B factor of the structure. Ramachandran plots (PROCHECK) (Laskowski et al., 1993), ERRAT (Colovos and Yeates, 1993), VERIFY 3D (Eisenberg et al., 1997), and SFCHECK (Vaguine et al., 1999) were used for model validation.

Gel Filtration Chromatography

Gel filtration experiments were performed on a Superdex 200 column (Amersham Biosciences) at a flow rate of 0.5 ml/min equilibrated with 10 mM HEPES (pH 7.5). For determination of molecular weights at various ionic strengths sodium chloride was included in the equilibration/running buffer and the experimental and standard protein sample buffers at concentrations of 20, 150, 300, and 600 mM. Mineralized AfFtn (500 Fe/tetraeicosamer) was prepared with minor modifications to the methods previously described (Liu et al., 2003). Mineralized protein samples where exchanged into 10 mM HEPES, 20 mM NaCl buffer (pH 7.5) prior to column loading. The following protein standards from Amersham Biosciences were used: chymotrypsinogen A (M_r 25,000), ovalbumin (M_r 43,000), bovine serum albumin (M_r 67,000), catalase (M_r 232,000), and ferritin (M_r 437 000).

Electron Microscopy

Carbon-coated parlodion support films mounted on copper grids were made hydrophilic immediately before use by high-voltage, alternating current glow discharge. Samples of mineralized ferritin (1 mg/ml) where exchanged into 10 mM HEPES buffer (pH 7.5) and applied directly onto grids and allowed to adhere for 2.5 min. Grids were rinsed with 3 drops of distilled water and stained with 1% uranyl acetate for 30 s. Specimens were examined in a Hitachi H-7000 electron microscope at an accelerating voltage of 75 kV. Images were recorded on Kodak electron microscope film 4489.

Supplemental Data

Supplemental Data is available online at http://www.structure.org/cgi/content/full/13/4/637/DC1/.

Acknowledgments

We thank the reviewers for their insightful comments. This work was supported by USPHS National Research Service Award GM07185 (E.J.), NIH GM31299-22 (D.C and M.G.), HHMI (M.S.), and NSF MCB-0345037 (I.S.). This work is based on research conducted at the Advanced Light Source at the Lawrence Berkeley National Laboratory, supported by the Director, Office of Science, Office of Basic Energy Sciences, Materials Sciences Division, of the U.S. D.O.E. (DE-AC03-76SF00098). This work is also based on research conducted at the UCLA-DOE X-Ray Crystallography Core Facility supported by DE-FC02-02ER63421. Toni Borders, Corie Ralston, Kim Ma, Chi-hee Kim, and Lejla Karamujic provided technical support.

Received: June 24, 2004
Revised: January 19, 2005
Accepted: January 20, 2005
Published: April 11, 2005

References

Almiron, M., Link, A.J., Furlong, D., and Kolter, R. (1992). A novel DNA-binding protein with regulatory and protective roles in starved *Escherichia coli*. Genes Dev. *6*, 2646–2654.

Andrews, S.C., Robinson, A.K., and Rodriguez-Quinones, F. (2003). Bacterial iron homeostasis. FEMS Microbiol. Rev. *27*, 215–237.

Archibald, F. (1983). *Lactobacillus plantarum*, an organism not requiring iron. FEMS Microbiol. Lett. *19*, 29–32.

Bothwell, T., and Mallett, B. (1955). The determination of iron in plasma or serum. Biochem. J. *59*, 599–602.

Carrondo, M.A. (2003). Ferritins, iron uptake and storage from the bacterioferritin viewpoint. EMBO J. *22*, 1959–1968.

Chasteen, N.D., and Harrison, P.M. (1999). Mineralization in ferritin: an efficient means of iron storage. J. Struct. Biol. *126*, 182–194.

Chayen, N.E., Shaw Stewart, P.D., Maeder, D.L., and Blow, D.M. (1990). An automated system for micro-batch protein crystallization and screening. J. Appl. Crystallogr. *23*, 297–302.

CCP4 (Collaborative Computational Project, Number 4)(1994). The CCP4 suite: programs for protein crystallography. Acta Crystallogr. D Biol. Crystallogr. *50*, 760–763.

Colovos, C., and Yeates, T.O. (1993). Verification of protein structures: patterns of nonbonded atomic interactions. Protein Sci. *2*, 1511–1519.

Cowtan, K., and Main, P. (1998). Miscellaneous algorithms for density modification. Acta Crystallogr. D Biol. Crystallogr. *54*, 487–493.

D'Arcy, A., Elmore, C., Stihle, M., and Johnston, J.E. (1996). A novel approach to crystallizing proteins under oil. J. Cryst. Growth *168*, 175–180.

Davis, M.E., Madura, J.D., Luty, B.A., and McCammon, J.A. (1991). Electrostatics and diffusion of molecules in solution: simulations with the University of Houston Brownian dynamics program. Comput. Phys. Commun. *62*, 187–197.

Doublie, S. (1997). Preparation of selenomethionyl proteins for phase determination. Methods Enzymol. *276*, 523–530.

Eisenberg, D., Luthy, R., and Bowie, J.U. (1997). VERIFY3D: assessment of protein models with three-dimensional profiles. Methods Enzymol. *277*, 396–404.

Esnouf, R.M., Ren, J., Garman, E.F., Somers, D.O.N., Ross, C.K., Jones, E.Y., Stammers, D.K., and Stuart, D.I. (1998). Continuous and discontinuous changes in the unit cell of HIV-1 reverse transcriptase crystals on dehydration. Acta Crystallogr. D Biol. Crystallogr. *54*, 938–953.

Gouet, P., Robert, X., and Courcelle, E. (2003). ESPript/ENDscript: extracting and rendering sequence and 3D information from atomic structures of proteins. Nucleic Acids Res. *31*, 3320–3323.

Ha, Y., Shi, D., Small, G.W., Theil, E.C., and Allewell, N.M. (1999). Crystal structure of bullfrog M ferritin at 2.8 A resolution: analysis of subunit interactions and the binuclear metal center. J. Biol. Inorg. Chem. *4*, 243–256.

Hempstead, P.D., Yewdall, S.J., Fernie, A.R., Lawson, D.M., Artymiuk, P.J., Rice, D.W., Ford, G.C., and Harrison, P.M. (1997). Comparison of the three-dimensional structures of recombinant human H and horse L ferritins at high resolution. J. Mol. Biol. *268*, 424–448.

Holden, J.F., and Adams, M.W. (2003). Microbe-metal interactions in marine hydrothermal environments. Curr. Opin. Chem. Biol. *7*, 160–165.

Hudson, A.J., Andrews, S.C., Hawkins, C., Williams, J.M., Izuhara, M., Meldrum, F.C., Mann, S., Harrison, P.M., and Guest, J.R. (1993). Overproduction, purification and characterization of the *Escherichia coli* ferritin. Eur. J. Biochem. *218*, 985–995.

Jones, T.A., Zou, J.Y., Cowan, S.W., and Kjeldgaard, M. (1991). Improved methods for building protein models in electron density maps and the location of errors in these models. Acta Crystallogr. A *47*, 110–119.

Kabsch, W., and Sander, C. (1983). Dictionary of protein secondary structure: pattern recognition of hydrogen-bonded and geometrical features. Biopolymers *22*, 2577–2637.

Kelley, L.A., MacCallum, R., and Sternberg, M.J.E. (1999). Recognition of remote protein homologies using three-dimensional information to generate a position specific scoring matrix in the program 3D-PSSM. In RECOMB 99, Proc. 3rd Ann. Conf. Comp. Mol. Biol. (New York: The Association for Computing Machinery), 218–225.

Kleywegt, G. (1996). Use of non-crystallographic symmetry in protein structure refinement. Acta Crystallogr. D Biol. Crystallogr. *52*, 842–857.

Kleywegt, G.J., and Jones, T.A. (1994). Detection, delineation, measurement and display of cavities in macromolecular structures. Acta Crystallogr. D Biol. Crystallogr. *50*, 178–185.

Laskowski, R.A., Moss, D.S., and Thornton, J.M. (1993). Main-chain bond lengths and bond angles in protein structures. J. Mol. Biol. *231*, 1049–1067.

Lawson, D.M., Artymiuk, P.J., Yewdall, S.J., Smith, J.M.A., Livingstone, J.C., Treffry, A., Luzzago, A., Levi, S., Arosio, P., Cesareni, G., et al. (1991). Solving the structure of human H ferritin by genetically engineering intermolecular crystal contacts. Nature *349*, 541–544.

Liu, X., Jin, W., and Theil, E.C. (2003). Opening protein pores with chaotropes enhances Fe reduction and chelation of Fe from the ferritin biomineral. Proc. Natl. Acad. Sci. USA *100*, 3653–3658.

Macedo, S., Romao, C.V., Mitchell, E., Matias, P.M., Liu, M.Y., Xavier, A.V., LeGall, J., Teixeira, M., Lindley, P., and Carrondo, M.A. (2003). The nature of the di-iron site in the bacterioferritin from *Desulfovibrio desulfuricans*. Nat. Struct. Biol. *10*, 285–290.

Martins, L., Huber, R., Huber, H., Stetter, K., Da Costa, M., and Santos, H. (1997). Organic solutes in hyperthermophilic Archaea. Appl. Environ. Microbiol. *63*, 896–902.

Murshudov, G.N., Vagin, A.A., Lebedev, A., Wilson, K.S., and Dodson, E.J. (1999). Efficient anisotropic refinement of macromolecular structures using FFT. Acta Crystallogr. D Biol. Crystallogr. *55*, 247–255.

Otwinowski, Z., and Minor, W. (1997). Processing of X-ray diffraction data collected in oscillation mode. In Methods in Enzymology, J. Carter and R.M. Sweet, eds. (New York: Academic Press), pp. 307–326.

Pereira, A.S., Tavares, P., Lloyd, S.G., Danger, D., Edmondson, D.E., Theil, E.C., and Huynh, B.H. (1997). Rapid and parallel formation of Fe3+ multimers, including a trimer, during H-type subunit ferritin mineralization. Biochemistry *36*, 7917–7927.

Perrakis, A., Morris, R., and Lamzin, V.S. (1999). Automated protein model building combined with iterative structure refinement. Nat. Struct. Biol. *6*, 458–463.

Posey, J.E., and Gherardini, F.C. (2000). Lack of a role for iron in the lyme disease pathogen. Science *288*, 1651–1653.

Santambrogio, P., Cozzi, A., Levi, S., Rovida, E., Magni, F., Albertini, A., and Arosio, P. (2000). Functional and immunological analysis of recombinant mouse H- and L-ferritins from *Escherichia coli*. Protein Expr. Purif. *19*, 212–218.

Schick, B., and Jurnak, F. (1994). Extension of the diffraction resolution of crystals. Acta Crystallogr. D Biol. Crystallogr. *50*, 563–568.

Schneider, T.R., and Sheldrick, G.M. (2002). Substructure solution with SHELXD. Acta Crystallogr. D Biol. Crystallogr. *58*, 1772–1779.

Stillman, T.J., Hempstead, P.D., Artymiuk, P.J., Andrews, S.C., Hudson, A.J., Treffry, A., Guest, J.R., and Harrison, P.M. (2001). The high-resolution X-ray crystallographic structure of the ferritin (EcFtnA) of *Escherichia coli;* comparison with human H ferritin (HuHF) and the structures of the Fe3+ and Zn2+ derivatives. J. Mol. Biol. *307*, 587–603.

Takagi, H., Shi, D., Ha, Y., Allewell, N.M., and Theil, E.C. (1998). Localized unfolding at the junction of three ferritin subunits. A mechanism for iron release? J. Biol. Chem. *273*, 18685–18688.

Theil, E.C. (1987). Ferritin: structure, gene regulation, and cellular function in animals, plants, and microorganisms. Annu. Rev. Biochem. *56*, 289–315.

Theil, E.C. (2001). Ferritin. In Handbook of Metalloproteins, A. Messerschmidt, R. Huber, T. Poulos, and K. Wieghardt, eds. (West Sussex, UK: John Wiley & Sons), pp. 771–781.

Touati, D. (2000). Iron and oxidative stress in bacteria. Arch. Biochem. Biophys. *373*, 1–6.

Vaguine, A.A., Richelle, J., and Wodak, S.J. (1999). SFCHECK: a unified set of procedures for evaluating the quality of macromolecular structure-factor data and their agreement with the atomic model. Acta Crystallogr. D Biol. Crystallogr. *55*, 191–205.

Vieille, C., and Zeikus, G.J. (2001). Hyperthermophilic enzymes: sources, uses, and molecular mechanisms for thermostability. Microbiol. Mol. Biol. Rev. *65*, 1–43.

Winn, M.D., Isupov, M.N., and Murshudov, G.N. (2001). Use of TLS parameters to model anisotropic displacements in macromolecular refinement. Acta Crystallogr. D Biol. Crystallogr. *57*, 122–133.

Zhao, G., Ceci, P., Ilari, A., Giangiacomo, L., Laue, T.M., Chiancone, E., and Chasteen, N.D. (2002). Iron and hydrogen peroxide detoxification properties of DNA-binding protein from starved cells. A ferritin-like DNA-binding protein of *Escherichia coli*. J. Biol. Chem. *277*, 27689–27696.

Accession Numbers

Structure factors and atomic coordinates for the native and iron bound structures have been deposited in the Protein Data Bank for release upon publication (ID codes 1S3Q, and 1SQ3, respectively).